01 Jan 2007

Demodulation of Fiber-Optic Sensors for Frequency Response Measurement

Abdeq M. Abdi

Steve Eugene Watkins
Missouri University of Science and Technology, watkins@mst.edu

Demodulation of Fiber-Optic Sensors for Frequency Response Measurement

Abdeq M. Abdi and Steve E. Watkins, *Senior Member, IEEE*

***Abstract*—The neural-network-based processing of extrinsic Fabry–Perot interferometric (EFPI) strain sensors was investigated for the special case of sinusoidal strain. The application area is modal or cyclic testing of structures in which the frequency response to periodic actuation must be demodulated. The nonlinear modulation characteristic of EFPI sensors produces well-defined harmonics of the actuation frequency. Relationships between peak strain and harmonic content were analyzed theoretically. A two-stage demodulator was implemented with a Fourier series neural network to separate the harmonic components of an EFPI signal and a backpropagation neural network to predict the peak-to-peak strain from the harmonics. The system performance was tested using theoretical and experimental data. The error for high-strain cases was less than about 10% if at least 12 harmonics were used. The frequency response of an instrumented cantilever beam provided the experimental data. The demodulator processing closely matched the actual strain levels.**

***Index Terms*—Fiber-optic strain sensors, modal testing, neural networks, smart structures.**

I. Introduction

SMART STRUCTURES technology combines a sensor or sensor networks with intelligent processing to monitor the environment of structure or react to structural changes [1]–[4]. The sensor choice and capabilities must be integrated with both the structure and the processing system to provide meaningful signal interpretation. Load-induced strain is an important measurand for structural applications since dimensional changes can be related to various performance, health, and safety issues. Fiber-optic-based systems have been developed that exploit the low profile and low loss of optic fiber [3]–[5]. Fiber-optic strain sensors based on Fabry–Perot etalons and Bragg grating structures [3], [4] have excellent capabilities for permanent, nondestructive testing in civil engineering [6], aerospace [7], [8], marine, and automotive structures. Their advantages include environmental ruggedness, temperature tolerance, low fatigue, and high sensitivity [3]–[10]. In particular, extrinsic Fabry–Perot interferometric (EFPI) strain sensors have been successfully applied in *in situ* strain sensing [5], [9], damage detection [10], and dynamic performance tests [7]. However, they are limited by specialized demodulation and signal processing requirements because the output response is periodic with strain [10]–[12]. The intelligent processing needs can be meet using artificial neural networks. These parallel computing architectures can accommodate complex and noisy signals from multiple sensors for pattern recognition, classification, and function approximation [13]. They have been used to process optical signals for impact, damage, fatigue, and performance assessment in structures [5]–[10].

A special case of strain sensing involves frequency response measurement. Modal analysis uses the resonant characteristics of a structure to provide information on its health and performance. Specific periodic excitation must be applied and sensor information collected. For instance, delamination, defects, and other damage has been characterized for composite structures [14]–[16]. Cyclic tests to determine fatigue also use sensor response to periodic excitation. The measurement of local strains during such tests, and particularly for failure or fatigue events, is useful. Example applications include bridges and propeller blades [7], [17]. Traditional resistive strain gages often fail as strain deltas and cycle counts increase. Alternatively, fiber-optic sensors show excellent fatigue characteristics and can be embedded for measurement of internal strain [18]. In addition to regulatory and quality assurance testing during development or installation, long-term health monitoring could be aided with a permanent intelligent system. Maintenance costs could be reduced as periodic inspections are done more easily and as quantitative information flags problems prior to severe or catastrophic failure.

Neural network processors have the ability to locate and classify damage using resonant frequencies measured in vibration tests [14]–[16]. Fiber-optic strain sensors can supply accurate information as high performance or permanent instrumentation, but the demodulation approaches for an EFPI system are limited by the signal nonlinearity. For sinusoidal actuation, a modal test using EFPI sensors can exploit the periodic modulation characteristic [19]. This research develops an intelligent demodulation processor that is simple and flexible. An EFPI-based health monitoring system has been proposed with an alternative neural-network approach [20]. While fast once trained, this demodulator is more complex and requires more preprocessing. A range of demodulation choices for EFPI-based modal or cyclic testing is needed to meet different application requirements.

This work reports the performance of a neural-network-based demodulation system for frequency response applications. This dedicated system is used to process the strain measured by EFPI sensors at high-strain levels. This demonstration of intelligent processing for a versatile sensor type can be applied to modal or

Manuscript received June 14, 2006; revised August 8, 2006; accepted September 1, 2006. The associate editor coordinating the review of this paper and approving it for publication was Dr. Subhas Mukhopadhyay.

A. M. Abdi is with Saada Optical, LLC, St. Louis, MO 63110 USA (e-mail: Abdeqa@aol.com).

S. E. Watkins is with Department of Electrical and Computer Engineering, University of Missouri–Rolla, Rolla, MO 65409-0040 USA (e-mail: steve.e.watkins@ieee.org).

Color versions of one or more of the figures in this paper are available online at http://ieeexplore.ieee.org.

Digital Object Identifier 10.1109/JSEN.2007.893238

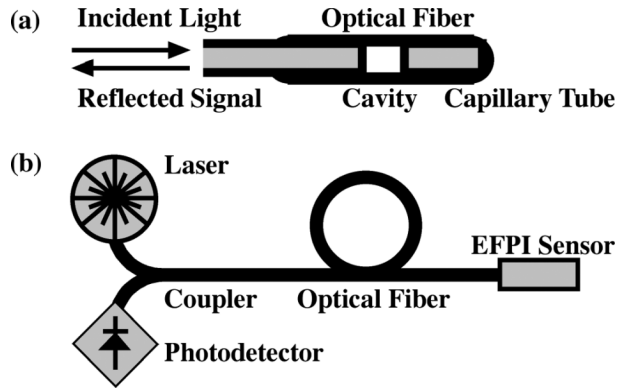

Fig. 1. Fiber-optic sensor system. (a) EFPI sensor. (b) Sensor instrumentation.

cyclic testing of structures and associated health monitoring. A sinusoidal strain is theoretically shown to produce well-defined harmonics in the nonlinear EFPI output signal for sensors with both low and high finesse. A Fourier series neural network is shown to separate the harmonic signal components and a back-propagation neural network to predict the peak-to-peak strain from the harmonics. A two-stage implementation was simulated with theoretical EFPI output data. The performance is compared for five and eight training sets containing 5, 6, and 12 harmonics of the EFPI signal as the peak-to-peak strain is varied from 10 to 200 $\mu\varepsilon$. The two-stage system was also implemented and tested with experimental data from an instrumented cantilever beam. The strain variation was again 10–200 $\mu\varepsilon$ and the frequency variation was 10–900 Hz. The actual frequency response for the beam is compared with that given by the processing system.

II. Fiber-Optic Strain Instrumentation and Harmonic Content

A. Extrinsic Fabry–Perot Interferometric (EFPI) Fiber-Optic Sensors

A Fabry–Perot interferometer utilizes multiple-beam interference in a cavity between two semireflective parallel surfaces and produces a transmittance (ratio of reflected irradiance I_r to incident irradiance I_i) [21]

$$\mathrm{I}_r/\mathrm{I}_i = \mathrm{F}\sin^2(\phi/2)/[1 + F\sin^2(\phi/2)]$$

where F is the cavity finesse (which depends on surface reflection) and ϕ is the round-trip phase between beams. This phase ϕ is $4\pi n_{\mathrm{opt}} d/\lambda$, where n_{opt} is cavity index, $d$is the distance between surfaces, and λ is the optical wavelength. Note that the transmittance is periodic with phase ϕ, and hence the modulation is nonlinear.

An EFPI fiber-optic sensor is shown in Fig. 1(a) where an air cavity $(n_{\mathrm{opt}} = 1)$ is formed between two polished end-faces of a single-mode fiber and a multimode fiber [9], [11], [12], [21]–[23]. A capillary tube is bonded to the two fibers and maintains the alignment of their end faces. The tube is bonded to a material under strain. The gage length is determined by the length of this capillary tube rather than the cavity and can be built to varying lengths. As the material and attached tube are strained, the reflected interference signal varies in response to changes in cavity spacing d and the strain is $\varepsilon = \Delta d/\mathrm{L}$, where L is the gage length. The period of the EFPI sensor response, i.e., the strain change per output fringe, is 1/2 the wavelength divided by the gage length. The peak-to-peak sensor output depends on the cavity finesse, i.e., a parameter related to end-face reflectances [21]. The sensor has little transverse coupling and effectively evaluates the axial component of strain [24]. The instrumentation for the EFPI sensor is shown in Fig. 1(b). A laser diode provides the optical input to the single-mode fiber. A coupler directs the light to the sensor and directs the reflected signal to a high-speed photodetector.

B. Harmonic Content of the EFPI Signal

A special case in strain measurement using EFPI sensor occurs for sinusoidal strain. The periodic sensor response modulates the sinusoidal strain. A sinusoidal strain excitation of this nonlinear response will produce a signal with components at the excitation angular frequency ω_m and its harmonics [19], [20], [25]. For a sinusoidal excitation, the phase is modulated as

$$\phi(t) = \phi_0 + (4\pi n_{\mathrm{opt}}/\lambda)\,\mathrm{L}\Delta\varepsilon\sin(\omega_m t + \theta_m)$$

where $\phi_0 = 4\pi n_{\mathrm{opt}} d/\lambda, \Delta\varepsilon$ is the peak strain, and ω_m and θ_m are angular frequency and phase of the excitation, respectively. The transmittance becomes

$$\begin{aligned}\mathrm{I}_r/\mathrm{I}_i &= \mathrm{F}\sin^2[\phi(t)/2]/\{1 + \mathrm{F}\sin^2[\phi(t)/2]\}\\ \mathrm{I}_r/\mathrm{I}_i &= \mathrm{F}\sin^2[(\phi_0/2) + (2\pi n_{\mathrm{opt}}/\lambda)\\ &\quad \mathrm{L}\Delta\varepsilon\sin(\omega_m t + \theta_m)]/\{1\\ &\quad + \mathrm{F}\sin^2[(\phi_0/2) + (2\pi n_{\mathrm{opt}}/\lambda)\\ &\quad \mathrm{L}\Delta\varepsilon\sin(\omega_m t + \theta_m)]\}\end{aligned}$$

This transmittance consists of well-defined harmonics of the excitation frequency. The weights vary with peak strain $\Delta\varepsilon$. For example, consider the transmittance for low finesse, i.e., small F [21]

$$\begin{aligned}\mathrm{I}_r/\mathrm{I}_i &\sim \mathrm{F}\sin^2[\phi(t)/2]\\ &= \mathrm{F}\sin^2[(\phi_0/2)\\ &\quad + (2\pi n_{\mathrm{opt}}/\lambda)\,\mathrm{L}\Delta\varepsilon\sin(\omega_m t + \theta_m)]\\ \mathrm{I}_r/\mathrm{I}_i &\sim (\mathrm{F}/2)\{1 - \cos[\phi(t)]\}\\ &= (\mathrm{F}/2)\{1 - cos[\phi_0 + (4\pi n_{\mathrm{opt}}/\lambda)\\ &\quad \mathrm{L}\Delta\varepsilon\sin(\omega_m t + \theta_m)]\}\\ \mathrm{I}_r/\mathrm{I}_i &\sim (\mathrm{F}/2) - (\mathrm{F}/2)\cos(\phi_0)\\ &\quad \{J_0[(4\pi n_{\mathrm{opt}}/\lambda)\,\mathrm{L}\Delta\varepsilon]\}\\ &\quad - (\mathrm{F}/2)\cos(\phi_0)\{2\Sigma_{n=1\text{ to }\infty}J_{2n}[(4\pi n_{\mathrm{opt}}/\lambda)\\ &\quad \times \mathrm{L}\Delta\varepsilon]\cos[(2n)(\omega_m t + \theta_m)]\}\\ &\quad + (\mathrm{F}/2)\sin(\phi_0)\{2\Sigma_{n=0\text{ to }\infty}J_{2n+1}[(4\pi n_{\mathrm{opt}}/\lambda)\\ &\quad \mathrm{L}\Delta\varepsilon]\sin[(2n+1)(\omega_m t + \theta_m)]\}\end{aligned}$$

The theoretical response was determined for an EFPI sensor $(n_{\mathrm{opt}} = 1)$ with a low finesse F of 0.15 (reflection coefficient of 0.04), an initial cavity spacing d of 101 μm, a gage length L of 8.00 mm, and a wavelength λ of 1300 nm. Fig. 2 shows an excitation signal of 100 Hz and a peak-to-peak strain of 200 $\mu\varepsilon$, the simulated EFPI response, and associated frequency content. A 200 μm excitation corresponds to a peak-to-peak change in

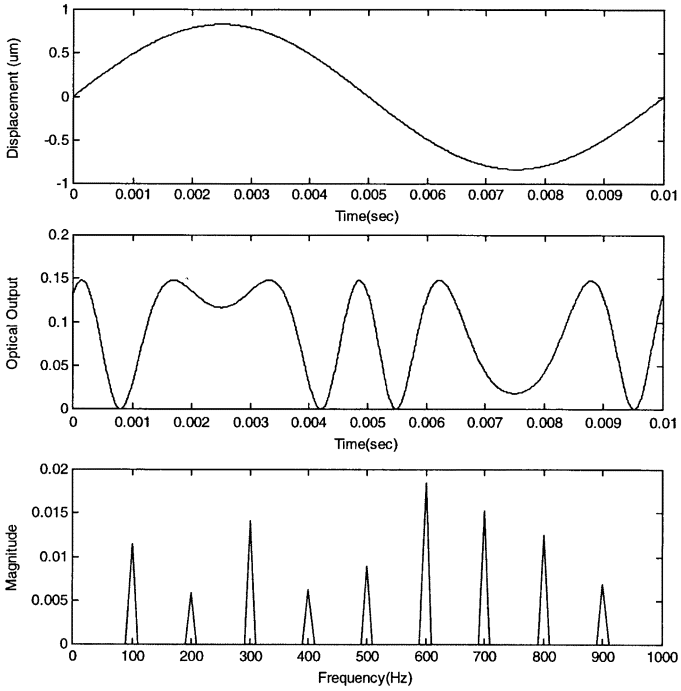

Fig. 2. (a) Strain excitation at 100 Hz and 200 $\mu\varepsilon$. (b) EFPI output for sinusoidal strain. (c) Fast Fourier transform of signal.

cavity distance of 1.66 μm. Sinusoidal strain also produces well-defined harmonic content using the full equation with higher values of finesse F [20], [25], as will be shown in the theoretical and experimental results.

III. Demodulation—Theoretical Implementation

A. Neural Network Implementation of Demodulation System

A two-stage demodulator is proposed that uses the time-domain signal directly from the EFPI system as an input and gives the peak-to-peak strain 2 $\Delta\varepsilon$ as the output. Sinusoidal excitation is assumed. The first stage consists of a Fourier Series Neural Network (FSNN) [26], [27] which determines the harmonics in the signal. The second stage consists of a backpropagation neural network (BPNN) which predicts the peak strain from the harmonics. (The peak strain(s) could be used by other processors, perhaps neural network based, to provide further intelligent functions [16].)

The FSNN is shown in Fig. 3. The inputs are the time-domain EFPI signal and the angular frequency of the excitation ω_1. This ADALINE network has 2 N activation neurons and a summer and is based on the Fourier series expansion

$$y(t) = \frac{1}{2}b_o + \sum_{n}^{N} [b_n \cos\omega_n t + c_n \sin\omega_n t]$$

where $y(t)$ represents the actual time-domain signal, b_n and c_n are the coefficients of the Fourier series expansion, ω_n is the angular frequencies of the harmonics (e.g., $\omega_n = n\omega_1$), and N is the total number of harmonics in the expansion. The FSNN creates an approximation signal

$$\hat{y}(t) = \frac{1}{2}W_o + \sum_{n}^{N} [W_n^c \cos\omega_n t + W_n^s \sin\omega_n t]$$

where W_n^c and W_n^s are the magnitude weights for the harmonics. A teaching algorithm continually adjusts the these weights to find the minimum error point using the Widrow–Hoff (Delta) learning rule

$$\begin{aligned} \Delta W_o &= \frac{1}{2}\alpha e_r \\ \Delta W_n^c &= \alpha e_r \cos\omega_n t \\ \text{and} \quad \Delta W_n^s &= \alpha e_r \sin\omega_n t \end{aligned}$$

where e_r is the error between $\hat{y}(t)$ and $y(t)$ and α is the learning rate with $0 < \alpha < 2/(N+1)$ [27]. Once the minimum error criterion is reached, the weights are passed as outputs for the N harmonics to the next stage. For the theoretical study, each harmonic had the cosine and sine weights, i.e., the W_n^c's and W_n^s's, and the FSNN had 2 N outputs. For the experimental study, each of the N harmonics are assigned the weight W_n

$$W_n = \sqrt{(W_n^c)^2 + (W_n^s)^2}$$

and the FSNN had N outputs, i.e., the W_n's. The use of W_n, rather than both cosine and sine weights, was necessary since the experimental storage configuration was limited to the combined parameter. The combined weight W_n facilitates use of a somewhat simpler neural network and instrumentation configuration.

The BPNN is triggered once the first stage meets the error threshold and uses the resulting harmonic weights. It had the W_n^c's and W_n^s's as the 2 N inputs for the theoretical study and the W_n's as the N inputs for the experimental study. The architecture had an input layer with four neurons, a hidden layer with eight neurons, and an output layer with one neuron. All activation functions are linear transfer functions. The gradient descent method was employed using random initial weights, momentum of 0.90–0.99, and a learning rate of 0.0154–0.0001 (the first parameter was for the theoretical data and the second for the experimental data). The BPNN was trained using inputs from the FSNN until the mean square error was less than 1 $\mu\varepsilon$. The output is the peak-to-peak strain $2\Delta\varepsilon$.

B. Data Simulation and Training

Theoretical data was simulated for training the BPNN and for testing the two-stage demodulator. EFPI signals were simulated using the full transmittance equation in Section II-B and used the parameters: optical index $n_{\text{opt}} = 1$, finesse $\text{F} = 0.49$ (reflection coefficient of 0.1), initial cavity spacing $d = 101$ μm, gage length $\text{L} = 8.31$ mm, wavelength $\lambda = 1300$ nm, and excitation frequency $f = 100$ Hz. Data sets were calculated for a peak-to-peak strain from 10 to 200 $\mu\varepsilon$ in steps of 5 $\mu\varepsilon$. The time-domain input signals for the FSNN were sampled with sampling frequency and the sampling points per waveform of 20 kHz and 600 points, respectively. The FSNN was tested with all of the data sets, since it requires no training and uses a dynamic teaching algorithm. Four versions of the BSNN were trained. In the first case (5th 5train), only the first five harmonics were considered and five distributed data sets were used. Hence, the FSNN produced 2 N or ten weights for the BSNN, i.e., the cosine and sine weights for each of the five harmonics. In the second case (6th 5train), the first

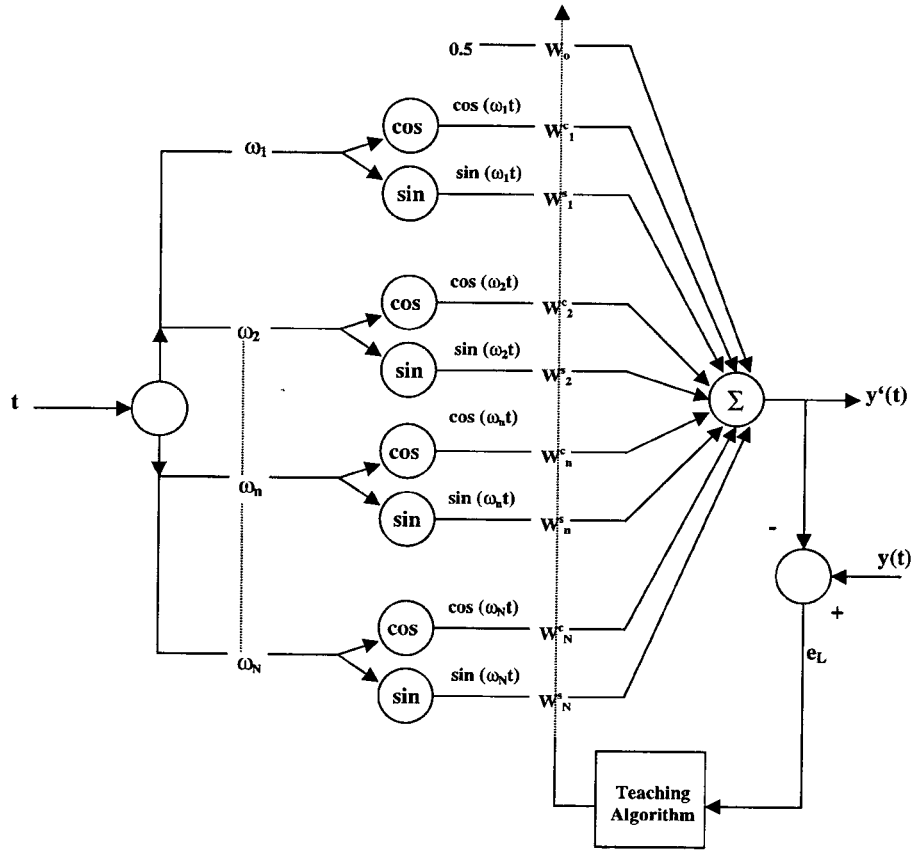

Fig. 3. Fourier series neural network architecture.

six harmonics are considered and again five data sets were used. In the third case (12th 5train), the first 12 harmonics are considered for 24 weights to the BSNN and again five training sets were used. In the fourth case (12th 8train), the first 12 harmonics are considered and eight training sets were used. The eight training sets corresponded to data at 10, 25, 50, 75, 100, 125, 165, and 200 $\mu\varepsilon$. In each case, the remaining theoretical data sets were used for testing with the appropriate number of harmonics considered.

C. Neural Network Test Results

Figs. 4–7 show the W_n harmonic magnitudes from the FSNN as a function of peak-to-peak strain for the first through the twelfth harmonic. The fundamental component is initially linear with strain as is expected for low-strain perturbations less than 50 $\mu\varepsilon$. The nonlinear components grow and the higher order harmonics become progressively more significant as strain increases. The relative magnitudes of the harmonic components closely matched that obtained from fast Fourier transforms of the EFPI signals. For example, the FSNN W_n magnitudes at 200 $\mu\varepsilon$ are 0.048813, 0.026333, 0.061728, 0.026827, 0.040688, 0.081441, 0.064022, 0.055386, 0.033921, 0.016497, 0.008265, and 0.001391 for harmonics 1–12, respectively. These relative magnitudes closely follow the fast Fourier transform harmonic content, as given in Fig. 2(c).

The BPNN was trained using 5, 6, or 12 harmonics and five or eight data sets, i.e., the cases identified as 5th 5train, 6th 5train, 12th 5train, and 12th 8train. Figs. 8 and 9 show the strain results and errors for the testing data sets with the two-stage demodulator. An increase in the number of harmonics considered and in the number of training sets improved the performance. The 12th 8train BPNN gave the best results in which a 7% error occurred for the low-strain levels, less than a 1% error for mid-strain levels, and about 2% error at high-strain levels. Note that the case with only five harmonics considered had a large error for high-strain levels at which the harmonic content was large, cf. Figs. 5–7.

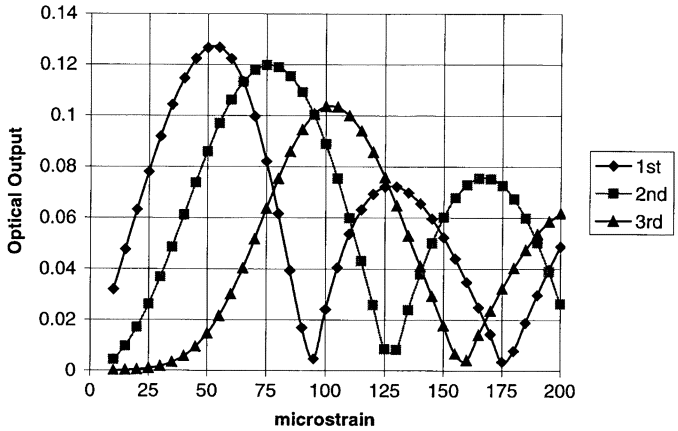

Fig. 4. First to third harmonic from Fourier series neural network for theoretical data.

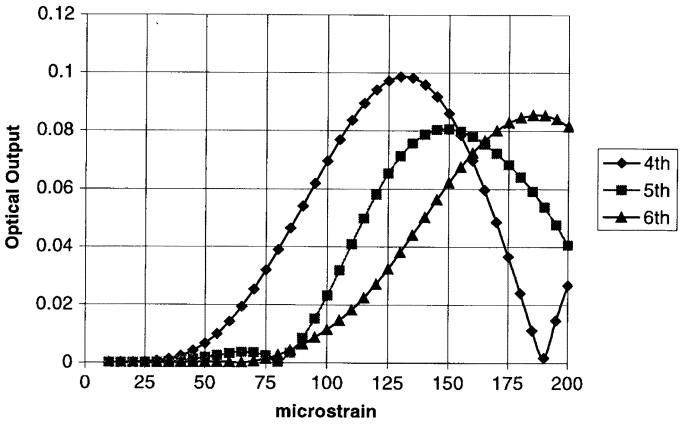

Fig. 5. Fourth to sixth harmonic from Fourier series neural network for theoretical data.

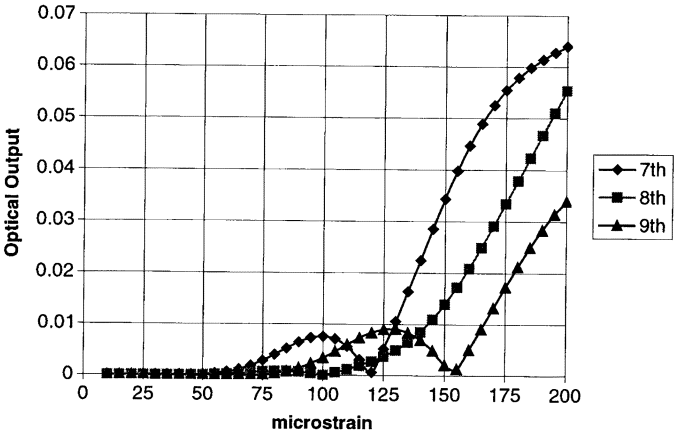

Fig. 6. Seventh to ninth harmonic from Fourier series neural network for theoretical data.

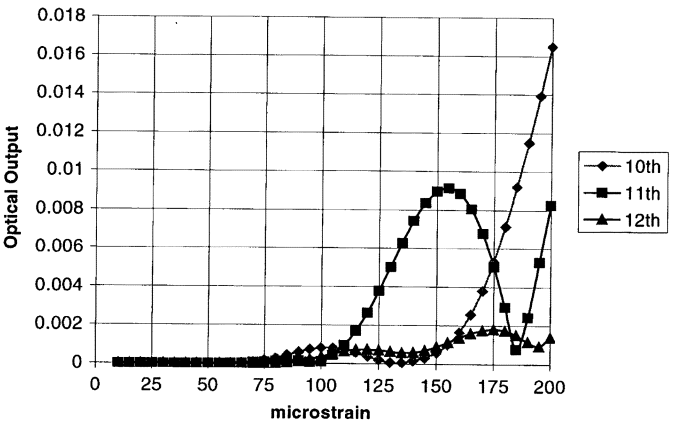

Fig. 7. Tenth to twelfth harmonic from Fourier series neural network for theoretical data.

A pseudofrequency response with five natural frequencies was created using mass-spring-damper models [25]. The response was designed to roughly approximate that of a beam as was used in the experimental part of this study. Corresponding

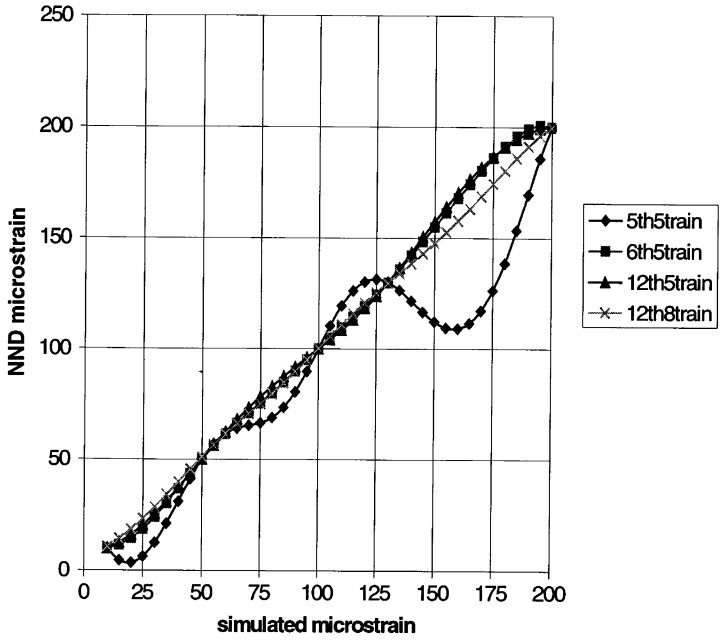

Fig. 8. Two-stage demodulator strain prediction compared with theoretical simulated strain. For the "XthYtrain" cases, the first through Xth harmonics were BPNN inputs and Y data sets were used for training.

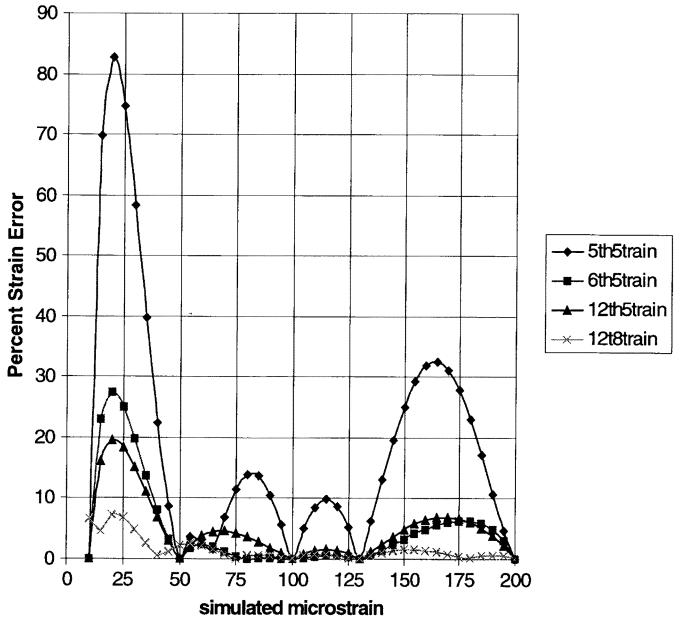

Fig. 9. Percent error in the demodulator as a function of simulated strain.

theoretical EFPI data sets were applied to the system to illustrate its behavior in this application. Fig. 10 shows the demodulator prediction using the 12th 8train BPNN. The frequency response was closely predicted except for the low-strain points, e.g., the response near minima for which strains were below 50 $\mu\varepsilon$. The largest error for the low-strain prediction was about 7%. For mid-strain and high-strain levels, the error was small at less that 2%.

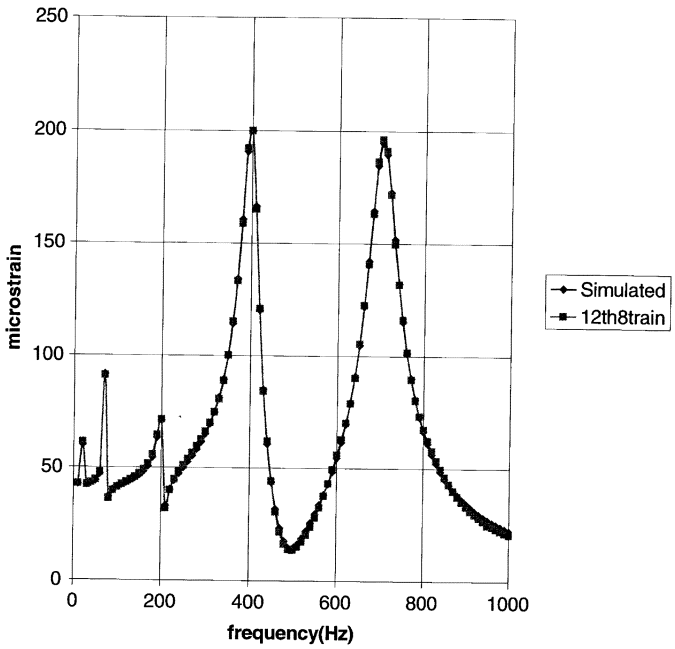

Fig. 10. Two-stage demodulator strain prediction compared with the theoretical pseudofrequency response.

IV. Demodulation—Experimental Implementation

A. Smart Beam System and Frequency Response Measurements

An instrumented cantilever beam was used in a frequency response test. This glass-epoxy composite beam contained eight laminated layers oriented $[0/90/0/90]_s$ degrees with respect to each other. (The part was used in the prior delamination study and contained no delaminations [16].) Its overall physical dimensions were 28.5 cm long, 2.5 cm wide, and 0.15 cm thick. It was fabricated from prepreg tapes using a Drake hydraulic hot press. The material properties were $E_{11} = 42.34$ GPa, $E_{22} = 11.72$ GPa, $G_{12} = 7.10$ GPa, $\nu_{12} = 0.27$, and $\rho = 1901.5$ kg/m^3. A cantilever clamp used 2.0 cm of the beam to give a cantilever length of 26.5 cm. A surface-mounted piezoelectric lead zirconate (PZT) ceramic actuator was located 3.5 cm from the clamp. A polyvinylidene fluoride (PVDF) sensor and a Luna Innovations model FOSS EFPI sensor, with an optical index $n_{\text{opt}} = 1$, a gap length of 101 μm, gage length of 8.31 mm, and a high finesse of 360 (reflection coefficient of 0.9) were placed on either side of the composite beam located 5.5 cm from its other end. The EFPI instrumentation was a Luna Innovations 1300-nm, FOSS support system, cf. Fig. 1(b).

Fig. 11 shows the experimental configuration. The beam was excited by the PZT and PZT amplifier through either the sinusoidal sweep output of a spectrum analyzer or the sinusoidal output of a programmable function generator. The strain output from the PVDF and EFPI sensors were displayed on an oscilloscope. EFPI calibration was performed using the PVDF sensor and applying fringe counting to selected EFPI signals [25], [28]. The EFPI output was also recorded with a storage oscilloscope and the spectrum analyzer. The measured frequency response of the beam is shown in Fig. 12 for low actuation levels using the PVDF sensor. High actuations produced the same natural frequencies. These frequencies were 12, 76.3, 211, 412, and 690 Hz.

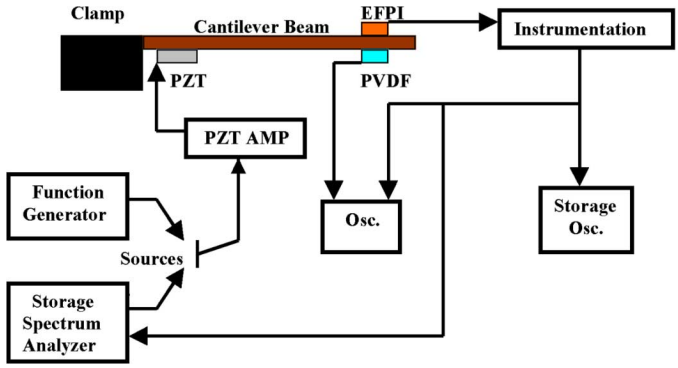

Fig. 11. Experimental configuration for the cantilever-beam frequency test.

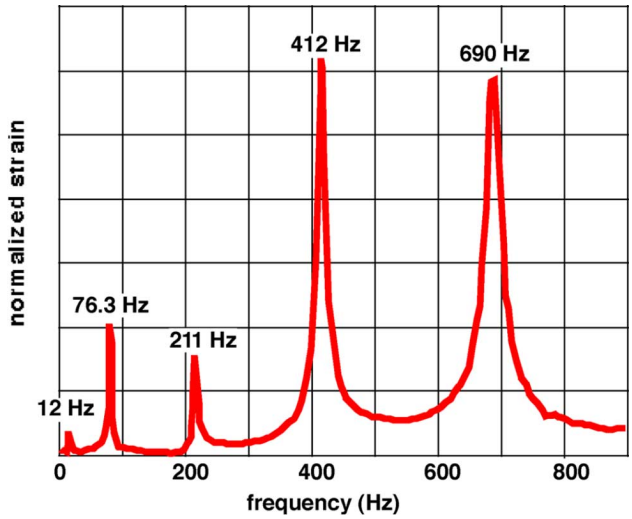

Fig. 12. Measured frequency response of the beam.

B. Neural Network Implementation, Experimental Data, and Training

The two-stage demodulator again consisted of the FSNN followed by the BPNN. For the experimental study, the FSNN produced the W_n's as the N inputs for the BPNN. Experimental data was taken for training the BPNN and for testing the two-stage demodulator. The testing consisted of comparing the convergence results for the FSNN and of the prediction results of the BPNN to the actual harmonics and strain levels, respectively. The BPNN was trained with eight experimental training sets that contained the first 12 harmonics of the EFPI signal, i.e., similar to the 12th 8train theoretical case.

Data sets were recorded at 690 Hz as the peak-to-peak strain varied between 10–200 $\mu\varepsilon$ in steps of 5 $\mu\varepsilon$. The excitation frequency of 690 Hz was chosen for the training since this natural frequency of the beam was the most stable. Eight of these sets were used for training and the rest for testing. The eight training sets corresponded to data at 10, 30, 55, 80, 105, 145, 175, and 200 $\mu\varepsilon$. In each case, the remaining theoretical data sets were used for testing with the appropriate number of harmonics considered. Also, the strains were measured for which the various harmonics reached local maxima and minima. Finally, the EFPI signals corresponding to the frequency response up to 900 Hz, i.e., through the first five natural frequencies, were

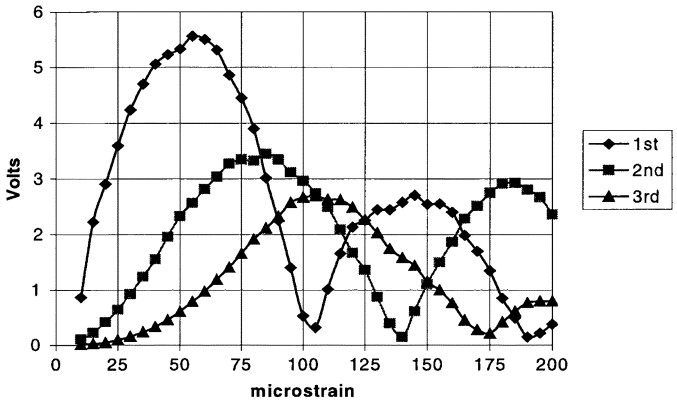

Fig. 13. First to third harmonic from Fourier series neural network for experimental data.

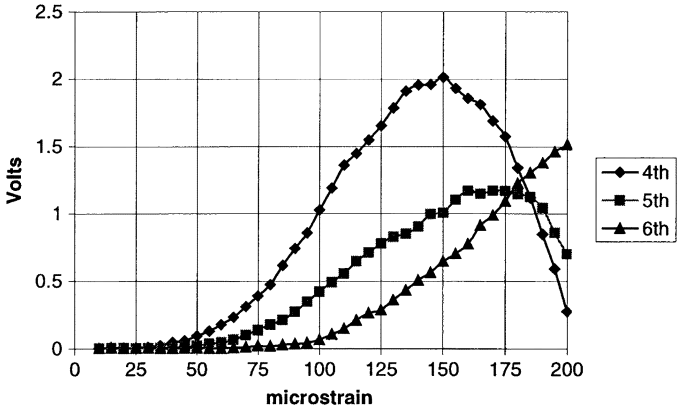

Fig. 14. Fourth to sixth harmonic from Fourier series neural network for experimental data.

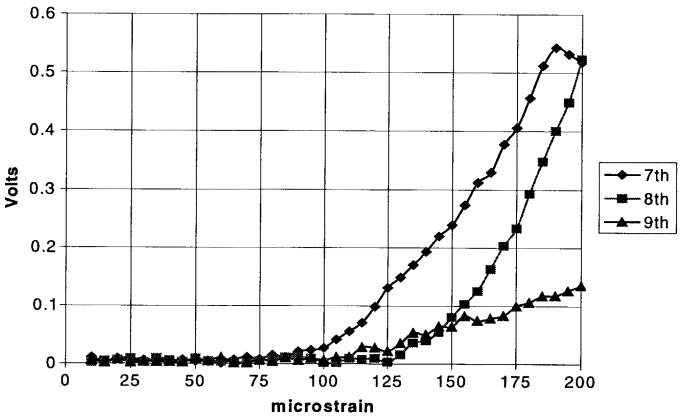

Fig. 15. Seventh to ninth harmonic from Fourier series neural network for experimental data.

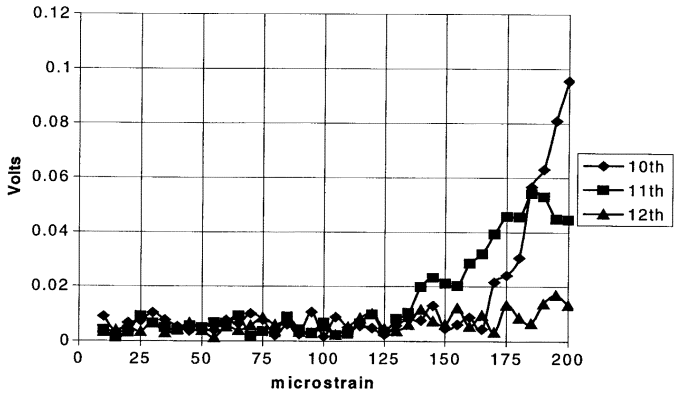

Fig. 16. Tenth to twelfth harmonic from Fourier series neural network for experimental data.

recorded. Note that these sets show the performance as strain is varied and as excitation frequency is varied. All experimental signal sets were operated on by the FSNN. No preprocessing or filtering were performed on the EFPI analog output except for amplitude normalization and digitization (100 000 samples/s); the analog output from the EFPI sensors has been shown to be relatively noise free [10], [16].

C. Neural Network Test Results

Figs. 13–16 show the W_n harmonic magnitudes from the FSNN for experimental data as a function of peak-to-peak strain for the first through the twelfth harmonics with an excitation of 690 Hz. The FSNN was able to converge to a clear minimum error point for all strain levels and gave a good representation of the experimental EFPI signal. While the relative harmonic magnitudes differ slightly, the strains corresponding to harmonic maxima and minima are very similar to the theoretical cases, cf. Figs. 4–7. Table 1 shows the comparison between the experimental and simulated theoretical curves.

The BPNN was trained using 12 harmonics and 8 data sets, i.e., the case identified as 12th 8train. Figs. 17 and 18 show the strain results and errors for the testing data sets with the two-stage demodulator. For all mid-strain and high-strain levels, the error was less than about 6%. Also, the demodulator frequency response shows good performance. Fig. 19 gives the predicted strain that closely reproduces the measured PVDF response, cf. Fig. 12. Fig. 20 shows the predicted strain (EFPI and demodulator) and the measured strain (PVDF) at each of the five natural frequencies of the beam. Neglecting the initial, small-magnitude natural frequency point, the strain level errors for the second through fifth natural frequencies are 2.4%, 15.2%, 15.8%, and 13.7%.

V. Conclusion

A two-stage neural network was developed to demodulate strain for EFPI strain sensors. The system was limited to sinusoidal strain measurement, but well-defined harmonic content of the EFPI signal was present for both small and large sensor finesse. The first stage employed a FSNN which determined the well-defined harmonics of an EFPI signal and the second stage used a BPNN which predicted the peak-to-peak strain from the harmonic information. The demodulation processor was trained and tested with both theoretical and experimental data. The correlation of predicted strain and actual strain was good with the best performance for mid-strain and high-strain levels. The approach was demonstrated with the cosine and sine harmonic coefficients and with the combined harmonic coefficient. This capability meets the needs of many structural monitoring applications. A typical frequency response measurement is illustrated

TABLE I
HARMONIC MAXIMA AND MINIMA FOR EXPERIMENTAL AND SIMULATED FSNN HARMONICS

Harmonic f = 690 Hz	Harmonic Condition	Experimental Strain Level	Simulated Strain Level	Percent Error
f	First Maxima	59 με	55 με	7.27
f	First Minima	100 με	92 με	8.69
f	Second Maxima	144 με	130 με	10.76
f	Second Minima	190 με	180 με	5.55
2f	First Maxima	85 με	76 με	11.84
2f	First Minima	140 με	128 με	9.37
2f	Second Maxima	183 με	168 με	8.92
3f	First Maxima	105 με	102 με	2.94
3f	First Minima	175 με	160 με	9.37
4f	First Maxima	145 με	130 με	11.53
4f	First Minima	205 με	190 με	7.89
5f	First Maxima	166 με	150 με	10.66
6f	First Maxima	200 με	185 με	8.10

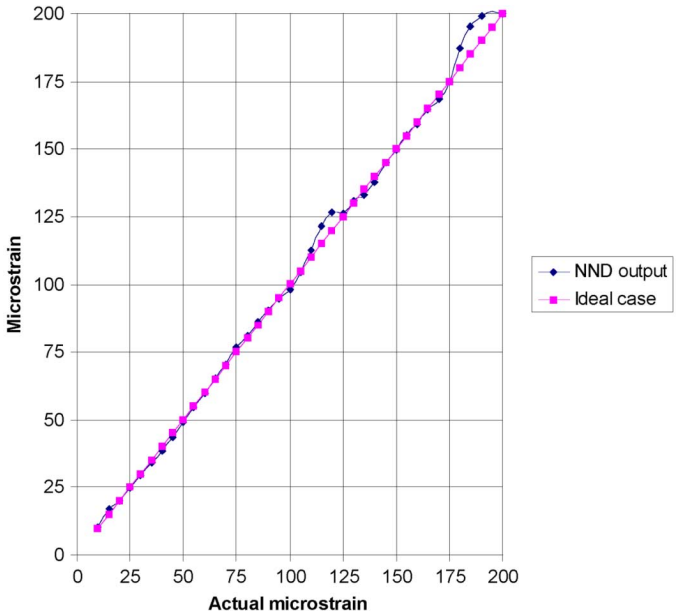

Fig. 17. Two-stage demodulator strain prediction of the experimental strain levels.

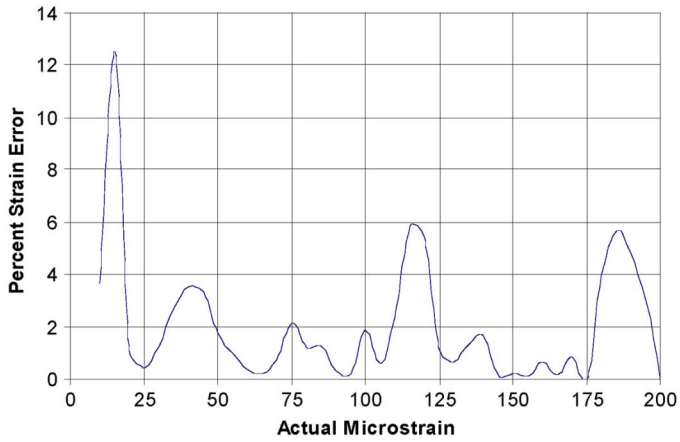

Fig. 18. Percent error in the demodulator as a function of experimental strain.

in Fig. 21. The demodulator can give rapid processing using just the excitation frequency and the EFPI sensor output.

The work demonstrated a simple and flexible approach for processing the signals from fiber-optic sensors using neural networks. The approach takes advantage of the amplitude modulation for EFPI sensors (and the simple associated support instrumentation) and exploits the periodic response with strain. For some dedicated applications, the total demodulation system may yield lower expense and speed advantages over fiber-optic systems based on the wavelength demodulation for Bragg sensors. EFPI sensor instrumentation can accurately measure dynamic strain in many extreme laboratory and field environments, but traditional demodulation techniques can be difficult to implement especially for dynamic events and can require complex processing. The FSNN and BPNN neural network architectures that are proposed here can be easily implemented in software or hardware. As an intelligent processing system, the demodulator can be rapidly trained with both theoretical or experimental data and can use the EFPI output directly with little or no preprocessing. The system must use sufficient harmonic content to represent the modulated EFPI signal (the higher the peak-to-peak strain, the more harmonics are needed). For the 200 $\mu\varepsilon$ case, 12 harmonics were necessary. Also, a relatively small number of training sets, i.e., eight sets, were required for good performance.

The target applications for the intelligent demodulator are modal tests and cyclic tests. Frequency response measurements can be linked to structural health and performance. Cyclic tests are needed to establish regulatory compliance and to assure quality behavior, e.g., fatigue. The experiment was limited to excitation frequencies below 900 Hz since only the first five harmonics are needed to assess this particular beam [16]. The approach should be effective for higher frequencies as long as the analog EFPI signal can be captured with sufficient

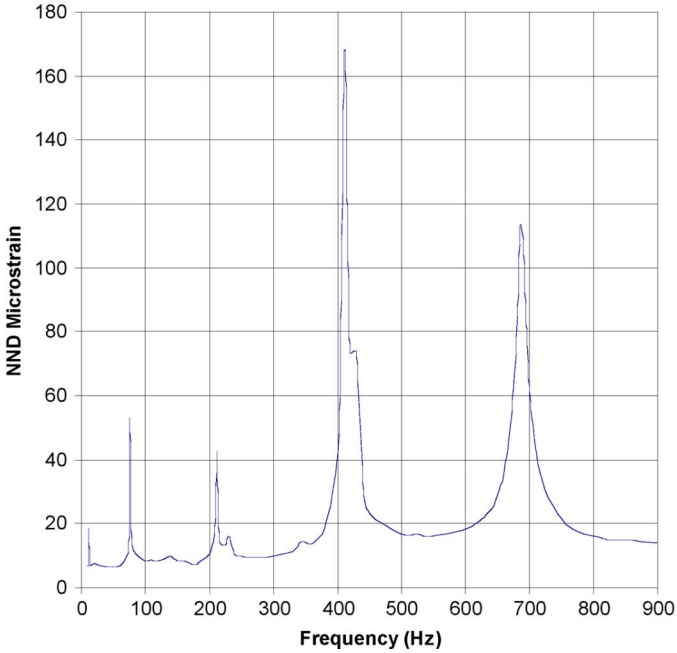

Fig. 19. Two-stage demodulator strain prediction of the experimental frequency response.

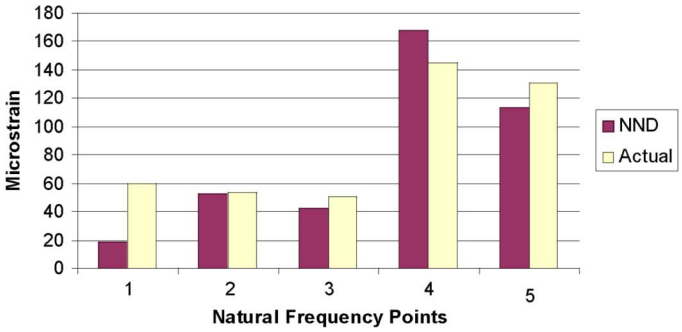

Fig. 20. Demodulator strain prediction at the natural frequencies compared to the measured strain levels.

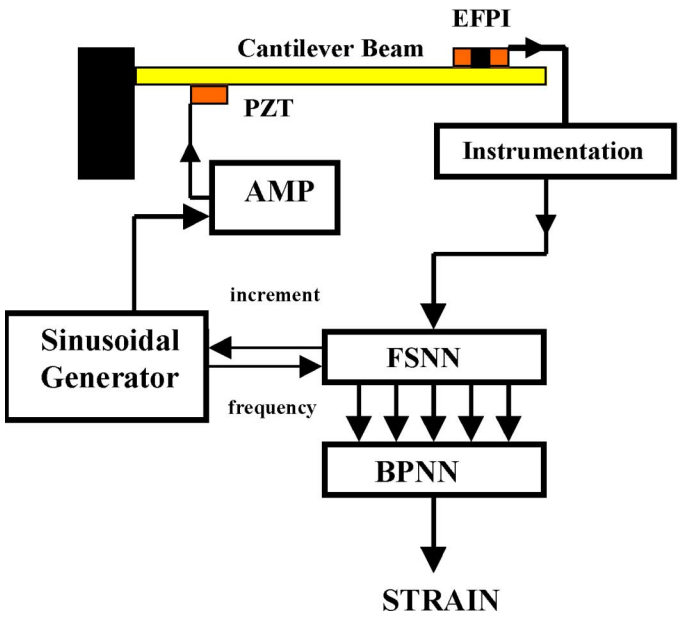

Fig. 21. Block diagram of the neural network demodulator applied to the frequency response measurement of an instrumented beam.

resolution. With an appropriate processing systems, smart structures can be implemented efficiently which use the EFPI as permanent, high-performance instrumentation for long-term monitoring. Further work toward this end will require refinement of the demodulator. The use of cosine and sine weights or the use of the combined harmonic coefficient will affect the required instrumentation and network complexity. The processing speed of a dedicated system and calibration procedures should be explored, as well as the number of harmonics and training data sets needed for varying levels of strain, especially higher strain levels. Also, the demodulator could be integrated with other higher level neural network processors to interpret structural parameters such health or fatigue [7], [16].

ACKNOWLEDGMENT

The authors are grateful for the technical assistance of Dr. Farhad Akhavan. They also thank Prof. K. Chandrashekhara who provided experimental support.

REFERENCES

[1] W. B. Spillman, Jr., "Sensing and processing for smart structures," in *Proc. IEEE*, Jan. 1996, vol. 84, no. 1, pp. 68–77.
[2] S. S. Chen and S. Kim, "Automated signal monitoring using neural networks in a smart structural system," *J. Intell. Material Syst. Structures*, vol. 6, pp. 508–515, 1995.
[3] E. Udd, "Fiber optic smart structures," in *Proc. IEEE*, Jan. 1996, vol. 84, no. 1, pp. 60–67.
[4] R. M. Measures, "Advances toward fiber optic based smart structures," *Opt. Eng.*, vol. 31, no. 1, pp. 34–47, 1992.
[5] D. G. Lee, M. Mitrovic, A. Friedman, and G. P. Carman, "Characterization of fiber optic sensors for structural health monitoring," *J. Composite Materials*, vol. 36, no. 11, pp. 1349–1366, 2002.
[6] S. E. Watkins, "Smart bridges using fiber optic sensors," *IEEE Instrum. Meas. Mag.*, vol. 6, no. 2, pp. 25–30, 2003.
[7] V. E. Zetterlind, III, S. E. Watkins, and M. Spoltman, "Fatigue testing of a composite propeller blade using fiber-optic strain sensors," *IEEE Sensors J.*, vol. 3, no. 4, pp. 393–399, Aug. 2003.
[8] A. Lunia, K. M. Isaac, K. Chandrashekhara, and S. E. Watkins, "Aerodynamic testing of a smart composite wing using fiber optic sensing and neural networks," *Smart Materials Structures*, vol. 9, no. 6, pp. 767–773, 2000.
[9] W. Zhao, J. Wang, A. Wang, and R. O. Claus, "Geometric analysis of optical fiber EFPI sensor performance," *Smart Materials Structures*, vol. 7, no. 6, pp. 907–910, 1998.
[10] F. Akhavan, S. E. Watkins, and K. Chandrashekhara, "Measurement and analysis of impact-induced strain using extrinsic Fabry–Perot fiber optic sensors," *Smart Materials Structures*, vol. 7, no. 6, pp. 745–751, 1998.
[11] D. Hogg, D. Janzen, T. Valis, and R. M. Measures, "Development of a fiber Fabry–Perot strain gauge," in *Proc. SPIE*, 1991, vol. 1588, pp. 300–307.
[12] K. A. Murphy, M. F. Gunther, A. M. Vengsarkar, and R. O. Claus, "Quadrature phase-shifted, extrinsic Fabry–Perot optical fiber sensors," *Opt. Lett.*, vol. 16, no. 4, pp. 273–275, 1991.
[13] M. T. Hagan, H. B. Demuth, and M. Beale, *Neural Network Design*, 6th ed. Boston, MA: PWS Publishing, 1996.
[14] P. C. Kaminiski, "The approximate location of damage through analysis of natural frequencies with artificial networks," in *Proc. Inst. Mechan., Eng. E*, 1995, vol. 209, pp. 117–123.
[15] A. C. Okafor, K. Chandrashekhara, and Y. P. Jing, "Delamination prediction in composite beams with built-in piezoelectric devices using modal analysis and neural networks," *Smart Materials Structures*, vol. 5, no. 2, pp. 338–347, 1996.
[16] S. E. Watkins, G. W. Sanders, F. Akhavan, and K. Chandrashekhara, "Modal analysis using fiber optic sensors and neural networks for prediction of composite beam delamination," *Smart Materials Structures*, vol. 11, no. 4, pp. 489–495, 2002.
[17] M. de Vries, M. Nasta, V. Bhatia, T. Tran, J. Greene, R. O. Claus, and S. Masri, "Performance of embedded short-gage length optical fiber sensors in a fatigue-loaded reinforced concrete specimen," *Smart Materials Structures*, vol. 4, no. 1A, pp. A107–A113, 1995.

[18] V. E. Zetterlind, III, S. E. Watkins, and M. W. Spoltman, "Feasibility study of embedded fiber-optic strain sensing for composite propeller blades," in *Proc. SPIE*, 2001, vol. 4332, pp. 143–152.
[19] K. A. Murphy, M. F. Gunther, R. O. Claus, T. A. Tran, and M. S. Miller, "Optical fiber sensors for measurement of strain and acoustic waves," in *Proc. SPIE*, 1993, vol. 1918, pp. 110–119.
[20] R. Dua, S. E. Watkins, and D. C. Wunsch, "Demodulation of extrinsic Fabry–Perot interferometric sensors for vibration testing using neural networks," *Opt. Eng.*, vol. 43, no. 12, pp. 2976–2985, 2004.
[21] M. Born and E. Wolf, *Principles of Optics*, 7th ed. Cambridge, U.K.: Cambridge Univ. Press, 2002.
[22] T. Yoshino, K. Kurasawa, and I. Katsuji, "Fiber-optic Fabry–Perot interferometer and its sensor applications," *IEEE J. Quantum Electron.*, vol. 10, pp. 1624–1633, 1982.
[23] A. D. Kersey, D. A. Jackson, and M. Corke, "A simple fiber Fabry–Perot sensor," *Opt. Commun.*, vol. 45, pp. 71–74, 1983.
[24] J. S. Sirkis, "Phase-strain-temperature model for structurally embedded interferometric optical fiber sensors with applications," in *Proc. SPIE*, 1991, vol. 1588, pp. 26–43.
[25] A. M. Abdi and S. E. Watkins, "Modal analysis using the bessel harmonics of an extrinsic Fabry–Perot interferometric sensor (EFPI) and neural networks," in *Proc. SPIE*, 2006, vol. 6167, no. 61671S.
[26] C. Zhu and F. W. Paul, "A Fourier series neural network and its application to system identification," *J. Dynamic Syst., Meas. Control*, vol. 117, pp. 253–260, 1995.
[27] J. F. Bouchard, C. Zhu, and F. W. Paul, "A neural network spectrum analyzer," *Mechatronics*, vol. 5, no. 6, pp. 20–29, 1995.
[28] A. M. Abdi and S. E. Watkins, "Four-point calibration of PVDF sensor using extrinsic Fabry–Perot interferometric (EFPI) sensor," in *Proc. SPIE*, 2003, vol. 5050, pp. 71–80.

Abdeq M. Abdi received the M.S. and B.S. degrees in electrical engineering from the University of Missouri–Rolla, in 1999 and 1997, respectively, and the Ph.D. degree in optical science from the University of Arizona, Tucson, in 2005.

He was previously employed by Corning. His research interests include health monitoring and sensor technology.

Dr. Abdi was the recipient of the University of Arizona Alfred P. Sloan Fellowship and a recipient of a GAANN Fellowship for 2001 and 2003.

Steve E. Watkins (S'80–M'90–SM'98) received the Ph.D. degree in electrical engineering from the University of Texas at Austin in 1989.

He is Director of the Applied Optics Laboratory and Professor of Electrical and Computer Engineering at the University of Missouri–Rolla. He has been an IEEE-USA Congressional Fellow for Congressman Dana Rohrabacher, a Visiting Physicist at Kirtland Air Force Base, and a Visiting Scholar at NTT in Japan. His research interests include smart structures and optical sensing systems.

He is a member of The International Society for Optical Engineers (SPIE), the Optical Society of America (OSA), and the American Society of Engineering Education (ASEE). He is on the Board of Governors for Eta Kappa Nu and the IEEE Intelligent Transportation Systems Society. He is the 2005 recipient of the IEEE Region 5 Outstanding Member Award, the 1999 recipient of the IEEE Region 5 Outstanding Engineering Educator Award, a 1993 finalist in the Eta Kappa Nu Outstanding Young Engineer Award Program, and a past National Science Foundation Graduate Fellow.